



Multi-functional fullerene soot/alumina composites with improved toughness and electrical conductivity

Andres E. Fals^a, Viktor G. Hadjiev^b, Francisco C. Robles Hernández^{a,*}

^a Department of Mechanical Engineering Technology, University of Houston, Houston, TX 77204-4020, USA

^b Texas Center for Superconductivity, Department of Mechanical Engineering, University of Houston, TX 77204-5002, USA

ARTICLE INFO

Article history:

Received 11 April 2012

Received in revised form

28 June 2012

Accepted 6 July 2012

Available online 13 July 2012

Keywords:

Ceramic

Composites

Mechanical alloying

Sintering

Nanostructured materials

Interfaces

ABSTRACT

We present the results of characterization and mechanical testing of alumina matrix composites reinforced with fullerene soot. The composites were manufactured by mechanical milling, sonication, and spark plasma sintering (SPS). Addition of 2 wt% Ni serves as an efficient catalyst for in situ transformation of soot into diamond and nanoparticles of fullerite and graphitic carbon during thermomechanical processing. The carbon nanostructures act as an effective reinforcement in the composite that results in an enhancement of the fracture toughness to 16.5 MPa m^{1/2}. Electrical resistivity decreases by 15 orders of magnitude. The improvement of composite properties is attributed to the formation of a homogeneous carbon coating on the alumina particles. The type of synthesized carbon nanostructures is shown to depend on the catalyst, SPS conditions, and the amount of fullerene soot added. A small amount of ruby is present as an impurity in the alumina, and serves as a convenient pressure sensor through its stress-dependent luminescence and gives additional multi-functionality to the composite.

Published by Elsevier B.V.

1. Introduction

A major goal in the development of ceramic matrix composites is to increase their toughness and in most cases their electrical conductivity. The main challenge of manufacturing ceramic matrix composites reinforced with carbon nanostructures is to achieve reinforcement percolation into the matrix [1]. Some of the successful efforts on this area for alumina matrix composites involve the use of different types of carbon nanotubes (CNTs): individual single-walled CNTs (SWCNTs) and ropes of SWCNTs, and multi-walled CNTs (MWCNTs) [2]. Ropes of SWCNTs have been successfully used to improve the fracture toughness of alumina by 300% (~9 MPa m^{1/2}), [2,3] while the electrical conductivity has been increased up to 13 orders of magnitude (to 100 S/m) at room temperature. Recently, graphene was used as reinforcement to toughen ceramic composites for aerospace and extreme environment applications [5]. Although these improvements of properties of ceramic composites seem significant, the values are still below those seen in most metals and alloys.

Material processing is crucial for preparing ceramic matrix composites with enhanced properties. Mechanical milling is widely used to manufacture nanostructured composites due to its ability to improve homogeneity, integrity and mechanical

properties [6,7]. Ideally, in order to preserve the nanostructured nature of the composites low temperature and for short times are recommended. These characteristics are mainly found in the spark plasma sintering (SPS) reaching theoretical (full densification) and preserves the nanostructured nature of the composites [8–11]. Some of the challenges to manufacture nanostructured carbon reinforced ceramic matrix composites include segregation, poor percolation, and cost.

Despite the successful use of SWCNT-ropes for reinforcement of alumina [2], CNTs are relatively expensive reinforcement and the use of much cheaper carbon soot for manufacturing of composites is desirable. This is possible through in situ transformation of carbon soot into other carbon nanostructures such as CNTs, diamond among other structures, by varying processing conditions [12].

In this paper we explore the use of carbon soot for reinforcement of alumina matrix along with the catalytic effect of transition metals to produce in situ carbon nanostructures. Transition metals, particularly nickel [13,14], have a strong catalytic effect and their use has been of crucial importance for mass production of CNTs. In order to keep the cost efficiency high we used the following simple manufacturing methods: mechanical alloying, sonication and spark plasma sintering (SPS). The characterization was conducted by means of Scanning electron microscopy (SEM), X-Ray Diffraction (XRD), Transmission electron microscopy (TEM), and Raman microscopy. Vicker's micro-hardness, Palmquist fracture toughness, density and porosity results are also reported. The Mode-I

* Corresponding author. Tel.: +1 713 743 8231; fax: +1 505 213 7106.

E-mail address: fcrobles@uh.edu (F.C. Robles Hernández).

fracture toughness K_{IC} in units $\text{MPa m}^{1/2}$ was determined by using the expression, $K_{IC} = 0.122(E/H_V)^{2/5}(L/al^{1/2})$ where E is the Young modulus, H_V is the Vicker's hardness, a and l are the indentation and crack lengths, respectively and L is the overall crack length.

2. Experimental

2.1. Materials

A commercial alumina (Al_2O_3) powder (98 wt% purity, mesh 140, all particles $< 106 \mu\text{m}$, and contained less than 0.005 wt% of heavy metals) was obtained from Sigma Aldrich. The fullerene soot containing less than 1 wt% of fullerenes (C_{60} and C_{70}) was purchased from the SERES Company. Nickel powder with a nominal purity of 99.9 wt% and a particle size of $3\text{--}7 \mu\text{m}$ was purchased from the Alfa Aesar. Two weight percent Ni was added to fullerene soot before milling.

2.2. Methods

Mechanical milling was conducted on batches of 1 and 10 g using a high energy, steel hardened, ball mill (SPEX) for 0, 0.5, 2, 5, 10, and 20 h for fullerene soot and 50 h for Ni powder. Alumina was SPEX milled for 20 h. After mechanical milling all the powders were sonicated to break up particle agglomeration and to enhance particle interactions. The milled and as synthesized powders were sonicated on a Misonix apparatus operated at $45\text{--}50 \text{ J/s}$ for 30 min.

The SPS operational conditions were temperature $600 \text{ }^\circ\text{C}$, $1300 \text{ }^\circ\text{C}$ and $1500 \text{ }^\circ\text{C}$, time $0\text{--}60 \text{ s}$ at a heating rate of $140 \text{ }^\circ\text{C/s}$. The average dimensions of the sintered samples were 12 mm in

diameter and 4 mm in thickness. The sintered products were polished following the standard metallographic procedures and were used for microhardness, electrical properties, and density testing. The micro-hardness test was conducted on a Future-Tech FX-7 Microhardness Tester using a load of 1 kN for 15 s. The reported values are the average of 9 measurements. The specific gravity was measured based on the Archimedes method using de-ionized water at standard conditions.

X-ray diffraction (XRD) was measured with a D5000 SIEMENS diffractometer equipped with a Cu tube and a characteristic $K_\alpha = 0.15406 \text{ nm}$ operated at 40 kV and 30 A. The SEM observations have been carried out on an FEI XL-30FEG on secondary electrons. Backscattering electrons and electron dispersive energy were conducted on a JEOL JSM-6400 SEM. The TEM/HRTEM has been conducted on a JEOL JEM200FXII. The Raman characterization was done on a confocal micro-Raman microscope XploRATM, Horiba JY. A 638 nm diode laser was used for excitation.

3. Results and discussions

3.1. Raw materials

Fig. 1(a)–(d) displays the electron micrographs of the raw materials. The fullerene soot shown in Fig. 1(a) has a fluffy appearance at micron length scale and under higher magnification (TEM) the particles reveal graphitic nanostructures and quasi-amorphous carbon as indicated by the respective electron diffraction pattern (Fig. 1(b)). Fig. 1(c) and (d) shows the Ni and alumina particles, respectively. The XRD characterization presented in Fig. 1(e) shows the structural characteristics of the raw materials in normalized intensity for better visualization.

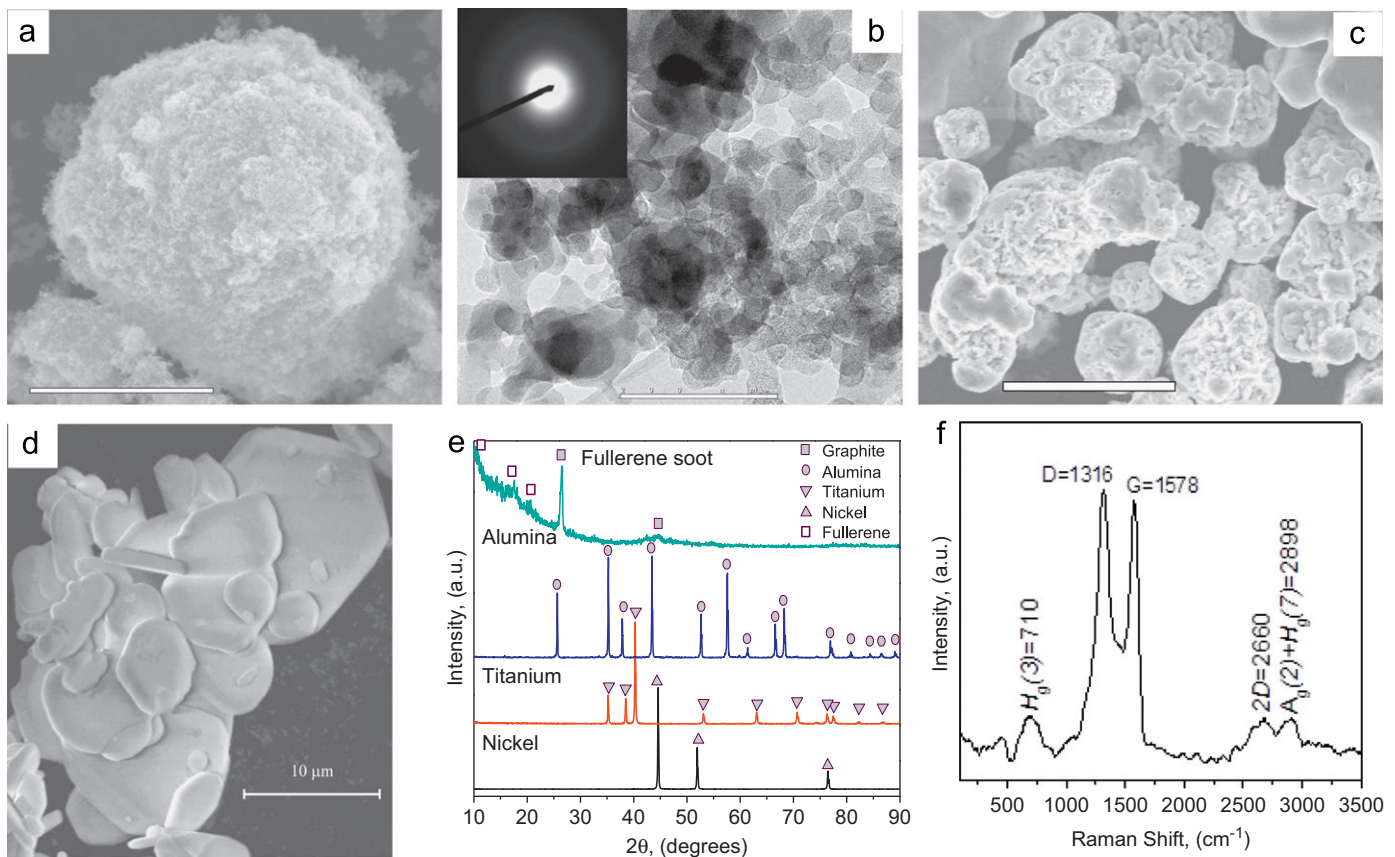


Fig. 1. (a) Scanning electron and (b) HRTEM micrographs of fullerene soot, (c) Ni mix, (d) Al_2O_3 , (e) XRD results of the raw materials, (f) fullerene soot integrated Raman spectrum excited with the 638 nm laser line.

Reflections in the fullerene soot (Fig. 1(b)) are wider than those of other compounds indicating a smaller size.

Fig. 1(f) shows an integrated, over large area, Raman spectrum of the fullerene soot. The characteristic Raman lines and bands of C_{60} and graphitic carbon are clearly discernible in the figure. One fundamental and one second-order combinational Raman lines of C_{60} are identified at 710 cm^{-1} ($H_g(3)$) and at 2898 cm^{-1} ($A_g(2)+H_g(7)$), respectively [15]. The intensity of the other Raman bands of C_{60} is weaker or hidden by more intense bands of the other forms of carbon. The Raman spectrum in Fig. 1(f) is dominated by the D, G and 2D bands of graphitic (sp^2) carbon measured at 1318 cm^{-1} , 1578 cm^{-1} , and 2660 cm^{-1} , respectively. Graphitic carbon may also contribute to the band at 2898 cm^{-1} through the D+G two-phonon scattering channel. Therefore, both Raman and XRD confirm that the fullerene soot contains mostly graphitic carbon and traces of fullerenes. We estimated that the average lateral size of graphitic particles is $L_a \sim 40\text{ nm}$ using the expression $L_a(\text{nm}) = 2.4 \times 10^{-10} L_{las}(I_G/I_D)$ [16], where $L_{las} = 638\text{ nm}$ is the excitation laser wavelength, and I_G and I_D are the Raman intensity of the D and G bands, respectively.

3.2. Mechanical milling

Fig. 2 displays the SEM micrographs of as milled products. The Al_2O_3 particles show refinement and the Ni particles are highly homogeneous. The milled fullerene soot particles are dense and no longer fluffy as the raw product. Fig. 2b is a backscattered image (compo-mode) of Ni powder with its respective energy dispersive x-ray spectrometry (EDS) demonstrating high homogeneity and

the sole presence of Ni in the as milled particles. The alumina was milled to break the particles seen in Fig. 1(d) to a particle size distribution that could improve densification.

Fig. 3 shows the Raman (a) and XRD (b) results for the fullerene soot in as purchased (raw) and milled conditions. The increase in intensity of the Raman signal for the 0.5 h and 2 h of Spex milled samples, also observed by XRD, is attributed to the "cold welding/annealing" [7] occurring during mechanical milling. After 2 h of milling the prevalent mechanism moves from welding to fracturing of graphitic particles. In the milled fullerene soot the D band develops a two-component lineshape with peak intensity shifting from 1318 cm^{-1} in raw fullerene soot to 1331 cm^{-1} in fullerene soot milled for 20 h (Fig. 3(a)). The latter is closer to the characteristic Raman frequency of diamond at 1332 cm^{-1} and suggests presence of diamond [17] particles that is also evident in the XRD data shown in Fig. 3(b).

The second-order Raman spectra of 0.5 h and 2 h milled fullerene soot are shown in Fig. 3(a). Three major bands are clearly seen in both the samples. The lowest frequency bands at 2429 cm^{-1} (0.5 h) and 2452 cm^{-1} (2 h) corresponds to D+D' phonon scattering, where D', typically at $\sim 1100\text{ cm}^{-1}$, is one of the low frequency defect induced bands in graphite and graphene. We relate the increased frequency of the D+D' band for the 0.5 and 2 h samples to the contribution from the second-order band of diamond [18,19]. The other two bands at $2667\text{--}2678\text{ cm}^{-1}$ and $2904\text{--}2932\text{ cm}^{-1}$ correspond to Raman scattering involving 2D and combinational D+G phonons, respectively. The intensity of the 2D bands in Fig. 3(a) is surprisingly strong for relatively disordered carbon, evidenced by the large I_D/I_G ratio. The 2D band intensity vanishes in amorphous (extremely

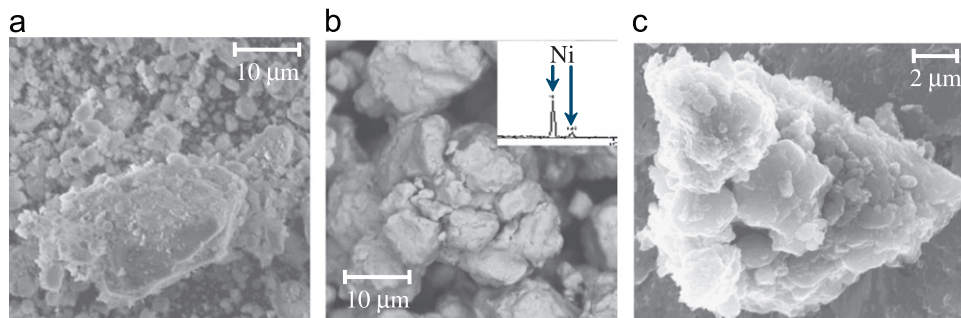


Fig. 2. Scanning electron micrographs for milled powders of (a) Al_2O_3 for 20 h, (b) Ni for 50 h and (c) fullerene soot for 50 h. The SEM micrograph for Ni was taken with backscattered electrons in compo-mode; the inset shows the EDS results.

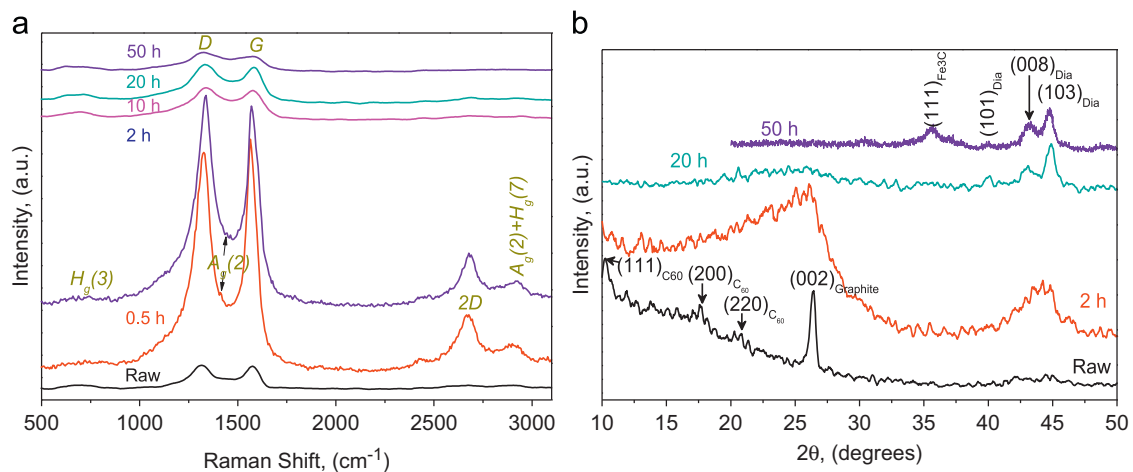


Fig. 3. (a) Raman and (b) XRD characterization of fullerene soot in RAW and Spex milled from 0.5 to 50 h. Notes: in (a) the Raman mainly shows the G and D bands typical of graphite, additionally the Hg_3 and Ag_2 bands of fullerene.

disordered) carbon. A possible explanation is that among the fractured graphitic particles there is a certain amount of graphene, where the first-order *D* and *G* bands are hidden by the broad disorder carbon bands. On the other hand, the 2D band of graphene is stronger in intensity than its *D* and *G* bands and may dominate the 2D spectra. Therefore, we see in the strong 2D bands, in the milled samples, an indication for a presence of graphene.

The XRD results of the mechanically milled fullerene soot powders are presented in Fig. 3(b). The main reflection in the raw fullerene soot corresponds to the (002) plane of graphite, the other reflections represent traces of C₆₀ fullerite (a molecular crystal made of C₆₀). For milling time longer than 2 h the presence of a new family of reflections, between 40 and 47 2θ°, is observed and these reflections become clearer with milling time. These reflections correspond to synthetic diamond with a hexagonal structure type *P6₃/mmc* previously identified in Refs. [18–20]. The XRD spectrum of the fullerene soot milled for 50 h shows Fe₃C reflections, but they are easily identifiable by means of Raman spectroscopy. Fe₃C is a byproduct contamination from the milling media.

3.3. Sintered composites

Fig. 4 shows the XRD results of the sintered alumina matrix composite samples reinforced with fullerene soot. The major findings are the in situ synthesized phases: diamond, fullerene, and graphite. The XRD reflection intensity of fullerene soot in the composites is weak, due to the small amount of fullerene soot (1, 2 or 5 wt% C), but the reflections are well discernible as shown in the central and right panel in Fig. 4.

In summary, SPS processing at 1300 °C for short time (1 min) sponsors the synthesis of diamond (Fig. 4(b)) while longer time (10 min) results in graphitization of part of the fullerene soot (Fig. 4(c)). Higher temperatures (1500 °C) and short time (1 min) are optimal to maximize the amount of synthesized diamond

(Fig. 4(d)). Lower temperatures (600 °C) are favorable for synthesis of fullerites (Fig. 4(e)). Comparing these results with the raw sample (Fig. 4(a)) one can conclude that the amount of diamond and fullerite increases during SPS. Additions of 2 wt% of fullerene soot in alumina sintered at 1500 °C for 1 min create a favorable conditions for synthesis of diamond (Fig. 4(d)), whereas in the composite containing 5 wt% fullerene soot, sintered at 1300 °C for 10 min, the fullerene soot is effectively graphitized (Fig. 4(c)). The amount of synthesized fullerite is maximized for the SPS sample at 600 °C with 2 wt% of fullerene soot (Fig. 4(e)). Further addition of fullerene soot (5 wt% and up) has no benefits on the synthesis of useful carbon species.

Fig. 5(a) presents the results of hardness testing of all the manufactured composites. The hardest composites are those produced with SPS for 1 min at 1500 °C with 1 and 2 wt% of fullerene soot. The average hardness of the SPS at 1500 °C composites is 14.6 GPa. This is 2–4 times higher than that reported for alumina membranes [21]. The hardness of the composites presented in this work average between 79% and 97% of the hardness reported for highly pure–highly dense alumina [22]. Therefore, the fullerene soot is considered as an effective reinforcement.

The hardness in the composites with 1 wt% fullerene soot sintered for 1 min at 1300 °C and 1500 °C is close to that of pure alumina (19 GPa) [23]. At the same sintering conditions but for composites containing 5 wt% fullerene soot the hardness decreases due to the partial transformation of fullerene soot into graphite (see e.g., Fig. 4(c)). On the other hand, the sintered samples with 1 wt% of fullerene soot in the absence of catalyst (Ni, Ti) show a drop in hardness to 2.67 GPa, the lowest hardness found in the investigated composites. This allows to conclude that Ni play an important role in hardness development and is potentially attributed to the formation of complex carbon nanostructures.

The porosity results of the composites are presented in Fig. 5(b). The sintering temperatures of 1300 °C and 1500 °C are

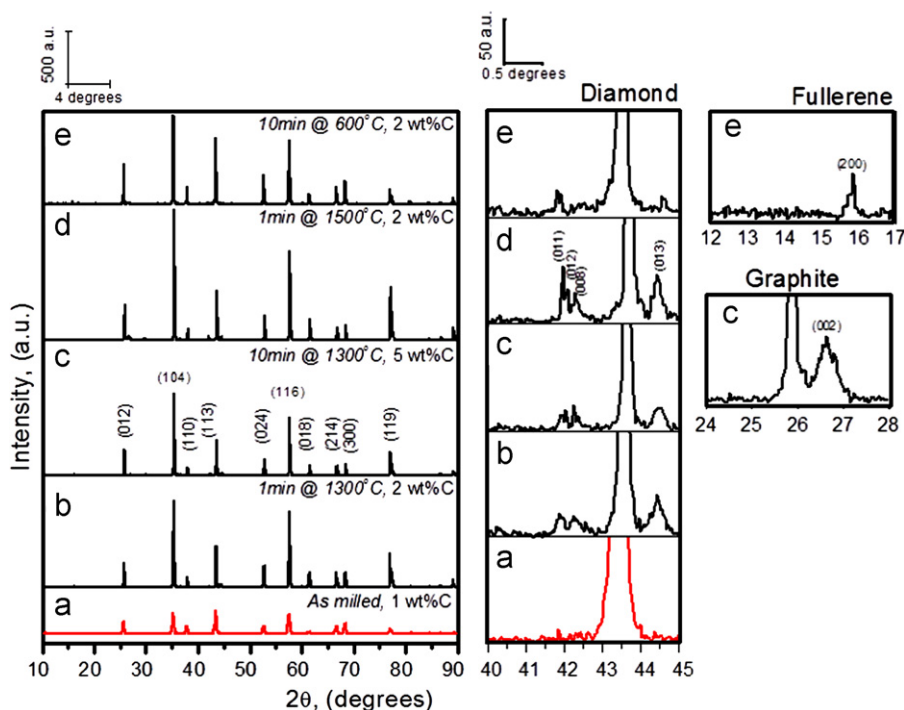


Fig. 4. XRD results of the alumina matrix composites SPS at different temperatures, times and amounts of fullerene soot: (a) As milled mix, (b–e) SPS treated samples at (b) 1300 °C for 1 min, (c) 1300 °C for 10 min, (d) 1500 °C for 1 min, and (e) 600 °C for 1 min. Central and right panels present selected diffraction angle ranges with XRD intensity zoomed 10 times.

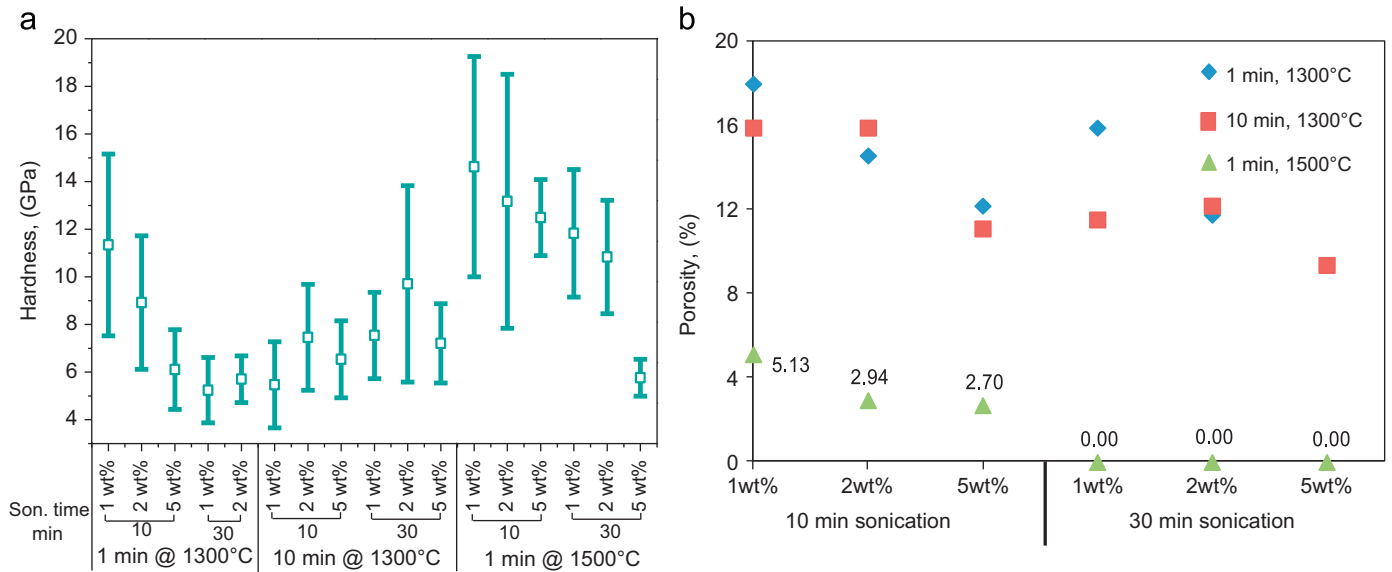


Fig. 5. (a) Hardness analysis of ceramic matrix composites reinforced with fullerene soot (a) and porosity (b) of the SPS composites.

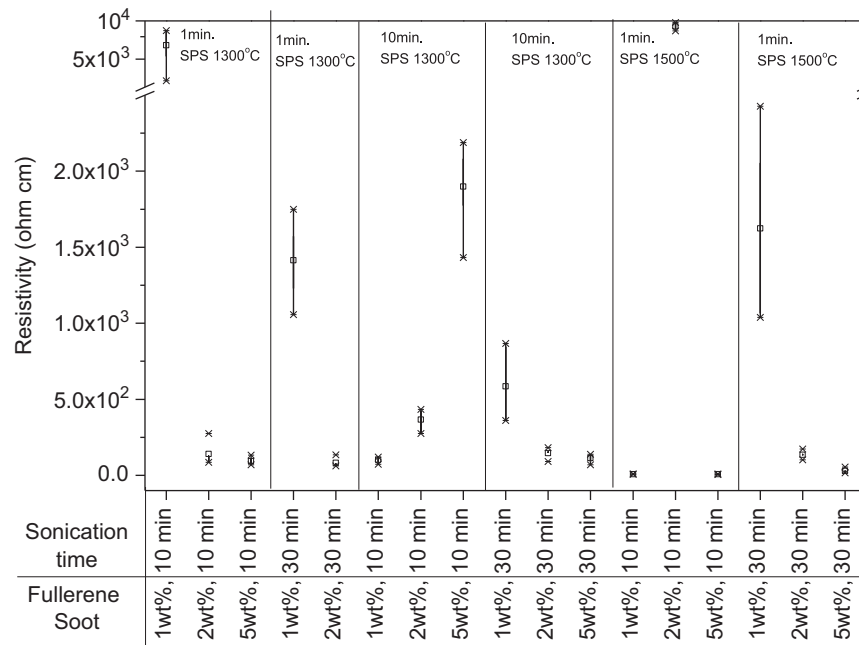


Fig. 6. Electrical resistivity of the SPS composites. Nomenclature for the labels: the first set of numbers expresses the percentage of fullerene soot and corresponding sonication time.

approximately 0.70–0.83 of the melting temperature of alumina in absolute scale. Sintering at 1500 °C for 1 min is enough to reach full densification in the composites made of components that were sonicated for 30 min, whereas in those sonicated for 10 min the porosity is larger. The composites prepared by SPS at 600 °C do not sinter and are in the form of loose powder. Sonication has a direct effect on densification due to the breakage of agglomerates formed during milling that otherwise remained unbroken during the sintering. Therefore, sonication is a way to improve the contact among the constituents and their percolation.

Fig. 6 shows the electrical resistivity results for the composites. Alumina has a resistivity between 1×10^{14} and $5 \times 10^{16} \Omega \text{ cm}$ depending on purity (from 95 to 99.8 wt%) and the atmospheric conditions (vacuum or air). The resistivity of the

composites presented in this work varies from $6 \Omega \text{ cm}$ to $6.5 \times 10^3 \Omega \text{ cm}$ at room temperature in air. This represents a reduction in resistivity between 13 and 15 orders of magnitude for the composites reinforced with 1 and 2 wt% of fullerene soot, respectively. The general trend is that the composite resistivity changes is trivial: it decreases with increasing fullerene soot content. Higher sintering temperatures further decrease the composite resistivity. Sonication and sintering times do not seem to have a direct effect on resistivity.

The fracture toughness values, reported here, correspond to selected samples because of the measuring procedure complications. For instance, some samples did not show the Palmqvist crack [25,26], while others chipped (Fig. 7) instead of cracked. Presumably the fracture toughness values in the samples without cracks are larger than the values reported herein and typically

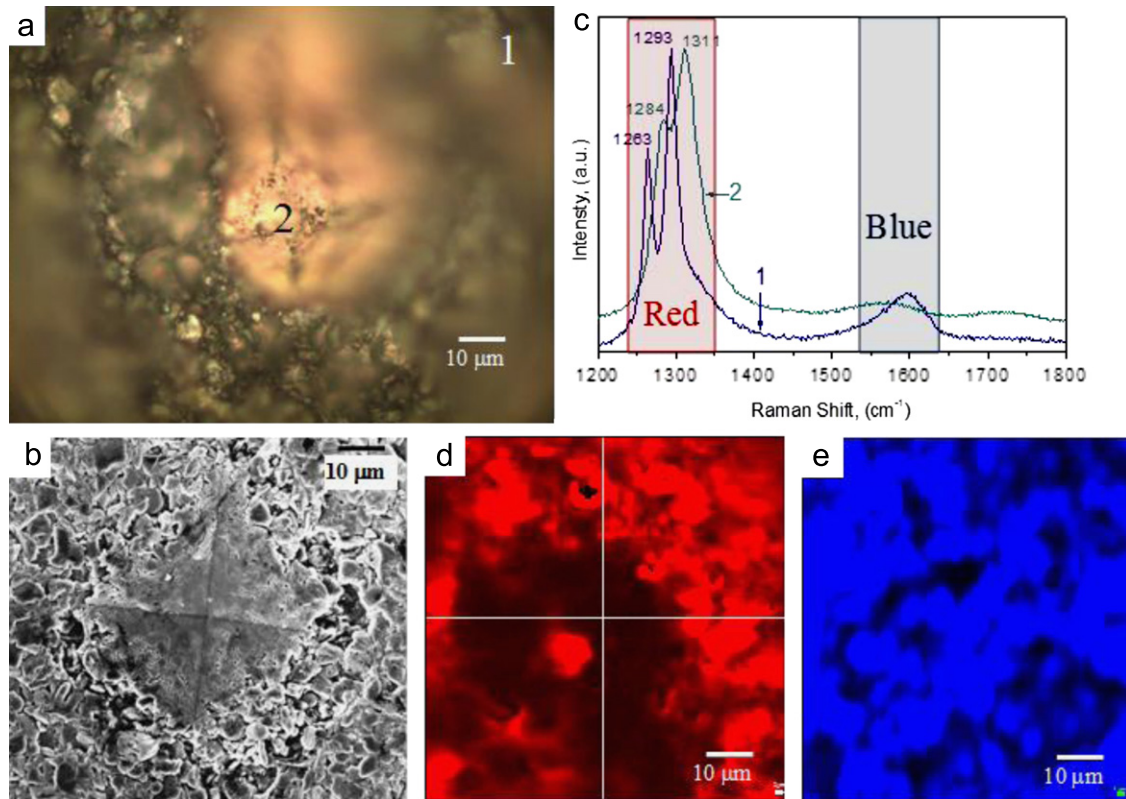


Fig. 7. (a) Microvickers indentation an respective (b) SEM micrograph of the Vicker's indentation , (c) Raman analysis for locations 1, 2, (d) map of predominance of Ruby (Red), (e) map of predominance of carbon (Blue). (For interpretation of the references to color in this figure legend, the reader is referred to the web version of this article.)

these are the highest density samples. The fracture toughness for the composites with 1 wt%, 2 wt%, and 5 wt% are 2.95, 16.5, and 9.5 MPa m^{1/2}, respectively. Notably, the fractures toughness observed in some of the samples showed an enhancement of up to 550% over that of pure alumina (2.9–3.4 MPa m^{1/2}) [27,28]. The use of CNTs and CNT ropes as reinforcement of alumina has been reported to improve the fracture toughness by 194% [3] and 300% [29], respectively.

Fig. 7 also presents a Raman mapping analysis carried over a micro-hardness Vicker's indentation. The Raman spectra of the alumina composite excited with the 638 nm laser line shown in Fig. 7(c) are dominated by a strong doublet at ~ 1260 cm⁻¹ and ~ 1290 cm⁻¹. These spectral line stems from ruby luminescence centers in the composite [30]. The ruby (Cr₂O₃) is formed as byproducts of the alumina due to the presence of traces of Cr (< 0.05 wt%) present in the alumina. The ruby luminescence is an optical emission involving transitions between the first excited ²E state and the ground ⁴A₂ state of Cr³⁺, the former split by the crystal field of oxygen atoms in the matrix. The crystal field splitting of ²E and the energy between ²E and ⁴A₂ states are sensitive to stresses and the monitoring of their shift with external pressure is commonly used in many pressure measurement techniques [30]. The two characteristic Cr³⁺ luminescence lines are found at 694.211 nm (1263 cm⁻¹) and 695.378 nm (1293 cm⁻¹), respectively, for the unstressed ruby [31]. Fig. 7(c) shows a difference in frequencies of the Cr³⁺ bands taken in the center of the indentation (residual stresses) and in unstressed regions. The ruby line frequency shifts from 1293.3 cm⁻¹ to 1311.1 cm⁻¹, in going from the unstressed region to the stressed region, which corresponds to a residual stress of approximately 1 GPa [30].

The improvements in toughness and conductivity in the composites are attributed to four main reasons: (i) the carbon

coating of the alumina particles, (ii) the formation of carbon nanostructures, (iii) crack propagation limited to transgranular mode of failure, and (iv) bridging effect of the graphene or graphitic particles. The above effects are presented in Fig. 8(a)–(c). The coating of the alumina particles is evident in Fig. 8(a) and (c) (compared to Figs. 1(d) and 2(a)). Presumably the growth of carbon nanofibers (Fig. 8(a)) was assisted by the catalytic effect of the added Ni particles. The necking and bridging observed in Fig. 8(c) helps preventing crack propagation and was previously reported in Ref. [5]. The strong decrease of electrical resistivity of alumina composites is mainly due to the nanostructured carbon network. Fig. 8(d) shows a HRTEM micrograph showing graphitic carbon decorated alumina particles demonstrating its effectiveness as reinforcement. The measured d-spacing (Fig. 8(d)) corresponds to that reported for graphitic carbon [32]. We believe that this type of carbon coating along the alumina improved the percolation among particles and resulted in the positive improvements in toughness and electrical conductivity reported herein.

4. Conclusions

Multifunctional alumina matrix composites reinforced with fullerene soot can be manufactured by consequent mechanical milling, sonication, and SPS. Fullerene soot is a good starting material for synthesis of the new carbon phases as diamond and fullerenes during mechanical milling and SPS. SPS treatments longer than 1 min transform the carbon species into graphite. Fullerene soot is also responsible for improvements of hardness, percolation, conductivity, densification, and fracture toughness. The optimal conditions for manufacturing of alumina matrix composite with enhanced mechanical and electrical properties are by using 2 wt% of fullerene soot sonicated for 30 min and

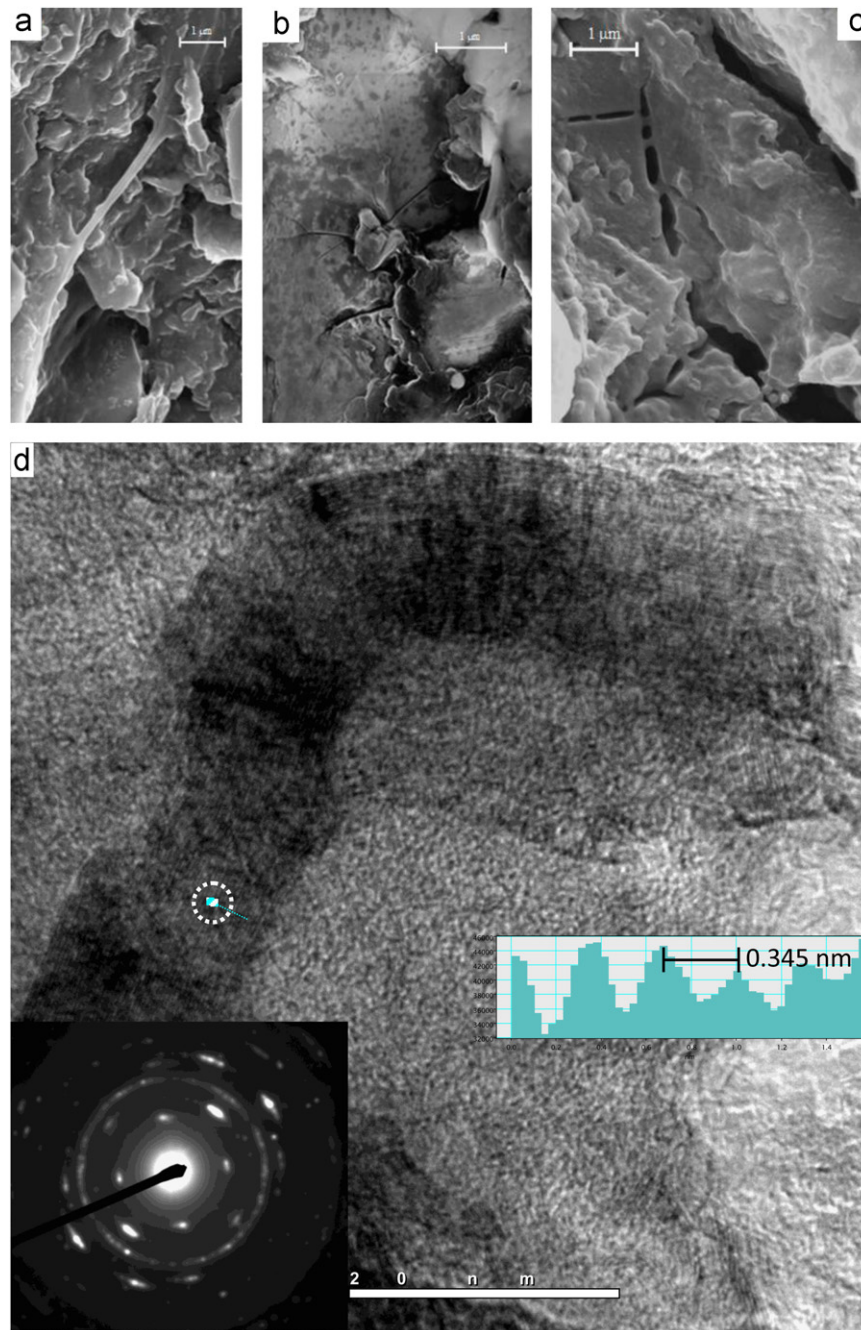


Fig. 8. Strengthening mechanisms of the alumina matrix composites by the fullerene soot reinforcements, (a,c) carbon coated matrix, (b,c) transgranular crack propagation, and (c) carbon nanoparticles bridging and preventing crack propagation (d) HRTEM of the composite showing an Al₂O₃ particle with its respective diffraction pattern and the D-spacing (0.344 nm) corresponding to graphitic carbon, measured at the location showing a dashed circle. The graphitic carbon is coating the alumina particles, the fullerene soot was spex milled for 50 h. The dotted line shows the location where the D-spacing was measured.

sintered for 1 min at 1500 °C. Produced composites are fully dense, having 15 orders of magnitude lower electrical resistivity, fracture toughness 500% higher than that of solid alumina, and 14.6 ± 4 GPa hardness.

Acknowledgments

Special thanks to the University of Houston and the government of Texas for the Start Up and HEAFS funding. The authors would like to express their gratitude to Dr. D. Butt for facilitating the Spark Plasma Sintering facilities at Center for the Advanced of Energy Studies (CAES) at Idaho Falls. Special thanks

to Dr. G. Majkic at the Mechanical Engineering Department (University of Houston) for his assistance to facilitate the micro-hardness equipment.

References

- [1] K. Ahmad, W. Pan, S.L. Shi, Appl. Phys. Lett. 89 (2006) 133122–133124.
- [2] G.D. Zhan, J.D. Kuntz, J.E. Garay, A.K. Mukherjee, Appl. Phys. Lett. 83 (2003) 1228–1230.
- [3] G.D. Zhan, J. Kuntz, J. Wan, J. Garay, A.K. Mukherjee, Scr. Mater. 47 (2002) 737–741.
- [5] L.S. Walker, V.R. Marotto, M.A. Rafiee, N. Koratkar, E.L. Corral, ACS Nano 5 (2011) 3182–3190.
- [6] P.S. Gilman, J.S. Benjamin, Annu. Rev. Mater. Sci. 13 (1983) 279–300.

- [7] C. Suryanarayana, Prog. Mater. Sci. 46 (2001) 1–184.
- [8] F.C. Robles-Hernández, H.A. Calderon, Mater. Chem. Phys. 132 (2012) 815–822.
- [9] F.C. Robles-Hernandez, H.A. Calderon, J. Met.—US 62 (2010) 63–68.
- [10] F.C. Robles Hernández, H.A. Calderón, in: H.A.C. Benavides (Ed.), MRS Conference, 2010, p. 5.
- [11] V. Garibay-Febles, H.A. Calderon, F.C. Robles-Hernández, M. Umemoto, K. Masuyama, Mater. Manuf. Processes 15 (2000) 547–567.
- [12] S. Arepalli, W.A. Holmes, P. Nikolaev, V.G. Hadjiev, C.D. Scott, J. Nanosci. Nanotechnol. 4 (2004) 762–773.
- [13] J.H. Hafner, M.J. Bronikowski, B.R. Azamian, P. Nikolaev, A.G. Rinzler, D.T. Colbert, K.A. Smith, R.E. Smalley, Chem. Phys. Lett. 296 (1998) 195–202.
- [14] X. Fan, R. Buczko, A.A. Puzos, D.B. Geohegan, J.Y. Howe, S.T. Pantelides, S.J. Pennycook, Phys. Rev. Lett. 90 (2003).
- [15] Z.H. Dong, P. Zhou, J.M. Holden, P.C. Eklund, M.S. Dresselhaus, G. Dresselhaus, Phys. Rev. B 48 (1993) 2862–2865.
- [16] L.G. Cancado, K. Takai, T. Enoki, M. Endo, Y.A. Kim, H. Mizusaki, A. Jorio, L.N. Coelho, R. Magalhaes-Paniago, M.A. Pimenta, Appl. Phys. Lett. 88 (2006).
- [17] S. Praver, R.J. Nemanich, Philos. Trans. R. Soc. A 362 (2004) 2537–2565.
- [18] S.A. Solin, A.K. Ramdas, Phys. Rev. B 1 (1970) 1687–1698.
- [19] S.A. Solin, A.K. Ramdas, Bull. Am. Phys. Soc. 14 (1969) 342–349.
- [20] P. Darrell Ownby, X. Yang, J. Liu, J. Am. Ceram. Soc. 75 (1992) 8.
- [21] Z. Xia, L. Riestler, B.W. Sheldon, W.A. Curtin, J. Liang, A. Yin, J.M. Xu, Rev. Adv. Mater. Sci. 6 (2004) 131–139.
- [22] A. Krell, P. Blank, J. Am. Ceram. Soc. 78 (1995) 1118–1120.
- [23] X. Wang, N.P. Padture, H. Tanaka, Nat. Mater. 3 (2004) 539–544.
- [25] A. Bravo-Leon, Y. Morikawa, M. Kawahara, M.J. Mayo, Acta. Mater. 50 (2002) 4555–4562.
- [26] S. Bhattacharya, A.R. Riahi, A.T. Alpas, Mater. Sci. Eng. A—Struct. 527 (2009) 387–396.
- [27] L.C. Lim, A. Muchtar, J. Mater. Sci. Lett. 21 (2002) 1145–1147.
- [28] C.C. Anya, S.G. Roberts, J. Eur. Ceram. Soc. 16 (1996) 1107–1114.
- [29] G.D. Zhan, J.D. Kuntz, J.L. Wan, A.K. Mukherjee, Nat. Mater. 2 (2003) 38–42.
- [30] K. Syassen, High Pressure Res. 28 (2008) 75–126.
- [31] J.K. Wright, R.L. Williamson, D. Rensch, B. Veal, M. Grimsditch, P.Y. Hou, R.M. Cannon, Mater. Sci. Eng. A—Struct. 262 (1999) 246–255.
- [32] S. Iijima, Nature 354 (1991) 56–58.